The Astrophysical Journal, 832:147 (8pp), 2016 December 1 doi:10.3847/0004-637X/832/2/147

OBSERVATIONS AND SIMULATIONS OF THE Na I D_1 LINE PROFILES IN AN M-CLASS SOLAR FLARE

D. Kuridze[1], M. Mathioudakis[1], D. J. Christian[2], A. F. Kowalski[4,5], D. B. Jess[1], S. D. T. Grant[1], T. Kawate[1], P. J. A. Simões[3], J. C. Allred[4], and F. P. Keenan[1]
[1] Astrophysics Research Centre, School of Mathematics and Physics, Queen's University Belfast, Belfast BT7 1NN, UK
[2] Department of Physics and Astronomy, California State University, Northridge, CA 91330, USA
[3] SUPA School of Physics and Astronomy, University of Glasgow, Glasgow G12 8QQ, UK
[4] NASA/Goddard Space Flight Center, Code 671, Greenbelt, MD 20771, USA
[5] University of Colorado, Boulder, CO 80303, USA
Received 2016 July 29; revised 2016 September 14; accepted 2016 September 22; published 2016 November 28

ABSTRACT

We study the temporal evolution of the Na I D_1 line profiles in the M3.9 flare SOL2014-06-11T21:03 UT, using observations at high spectral resolution obtained with the Interferometric Bidimensional Spectrometer instrument on the Dunn Solar Telescope combined with radiative hydrodynamic simulations. Our results show a significant increase in the intensities of the line core and wings during the flare. The analysis of the line profiles from the flare ribbons reveals that the Na I D_1 line has a central reversal with excess emission in the blue wing (blue asymmetry). We combine RADYN and RH simulations to synthesize Na I D_1 line profiles of the flaring atmosphere and find good agreement with the observations. Heating with a beam of electrons modifies the radiation field in the flaring atmosphere and excites electrons from the ground state $3s\ ^2S$ to the first excited state $3p\ ^2P$, which in turn modifies the relative population of the two states. The change in temperature and the population density of the energy states make the sodium line profile revert from absorption into emission. Furthermore, the rapid changes in temperature break the pressure balance between the different layers of the lower atmosphere, generating upflow/downflow patterns. Analysis of the simulated spectra reveals that the asymmetries of the Na I D_1 flare profile are produced by the velocity gradients in the lower solar atmosphere.

Key words: methods: numerical – radiative transfer – Sun: chromosphere – Sun: flares – Sun: photosphere – techniques: imaging spectroscopy

Supporting material: animation

1. INTRODUCTION

The lower solar atmosphere is key to our understanding of solar flares, because the vast majority of the radiative energy of flares originates in the chromosphere and photosphere. Chromospheric radiation is dominated by the optically thick lines of hydrogen, calcium, and magnesium that provide diagnostics on flare dynamics. One of the main characteristics of the flaring chromosphere is the centrally reversed Hα emission profile with asymmetric red and blue wings. The asymmetries are attributed to the downflow and upflow of plasma, triggered by the deposition of nonthermal energy, which are also known as chromospheric condensation and evaporation (Ichimoto & Kurokawa 1984; Wuelser & Marti 1989; de la Beaujardière et al. 1992). These processes can be very effective tracers for the velocity field of the flaring atmosphere. Abbett & Hawley (1999) computed flare time-dependent Hα and Ca II K line profiles with the radiative hydrodynamic code (RADYN; Carlsson & Stein 1997), and showed that the asymmetries could be produced by the strong velocity gradients generated during the flare. These gradients create differences in the opacity between the red and blue wings of Hα and their sign determines whether the asymmetric emission appears to the blue or red side of the line profile. Recently, Kuridze et al. (2015) made a direct comparison of the observation and RADYN simulation for the evolution of the Hα profile. They showed that the steep velocity gradients in the flaring chromosphere modify the wavelength of the central reversal in Hα. The shift in the wavelength of maximum opacity to shorter and longer wavelengths generates the red and blue asymmetries, respectively.

The exact formation height of the Na I D_1 line core is difficult to estimate from observations; simulations indicate that it is formed below the formation height of the Hα, Ca II H & K, and the Ca II infrared (IR) triplet line cores (Finsterle et al. 2004). Simoniello et al. (2008) explored the formation height of the Na I D lines by calculating the response functions of their profiles to p-mode power variations. They concluded that the line has its origin in a wider region, from the photosphere up to the lower chromosphere at a height of around 800 km.

Observations and simulations performed for the quiet solar atmosphere have revealed that the Na I D_1 core brightness samples the magnetic bright points in the solar photosphere and is strongly affected by 3D resonance scattering (Moretti et al. 2002; Jess et al. 2010; Leenaarts et al. 2010). These studies suggest that the line core emission in the quiet Sun originates in the upper photosphere and lower chromosphere.

There is a lack of flare observations and modeling in the Na I D lines, with the exception of some early work (Gurtovenko 1967; Falchi et al. 1990; Montes et al. 1996). The most recent observations of solar flares in Na I D_1 have been reported by Cessateur et al. (2010), who analyzed the D_1 and D_2 line intensities observed with the GOLF spectrophotometer on board the *Solar and Heliospheric Observatory* (*SOHO*). They found that the intensities of these lines integrated over the solar disk are increased during flares. However, the GOLF instrument can only record intensities in the single wavelength positions of ± 0.108 Å from the line core and does not allow for full spectral line profiles.

In this paper we present observations at high temporal, spatial, and spectral resolution of an M3.9 solar flare in Na I

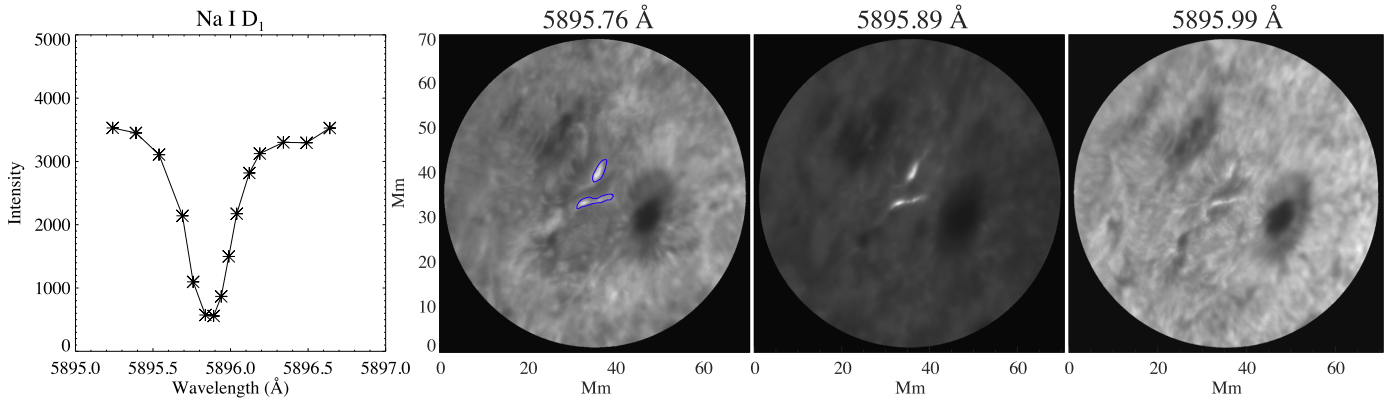

Figure 1. IBIS Na I D_1 line profile of a quiet solar region. Asterisks show the spectral positions selected for the IBIS line scan. The full black line shows the mean spectrum averaged over the field of view (FOV) of the quiet Sun. Na I D_1 wing and core images at selected wavelength positions. The temporal evolution is shown in the movie available online. The blue contours show the upper and lower flare ribbons analyzed in this paper. Contours indicate the 50% level of the intensity maximum.

(An animation of this figure is available.)

D_1. Multi-wavelength observations of this M3.9 flare are also presented in D. J. Christian et al. (2016, in preparation). We study the evolution of the line profiles of the flare ribbons, and compare our findings with synthesized profiles obtained with a radiative hydrodynamic simulation. Motivated by the close match between simulations and observations, we investigate the formation of centrally reversed, asymmetric Na I D_1 line profiles using synthetic spectra. The line contribution functions and the velocity field in the simulated atmosphere allow us to investigate the nature of the observed line asymmetries.

2. OBSERVATIONS AND DATA REDUCTION

The observations presented in this work were obtained between 19:20 and 21:27 UT on 2014 June 11 with the Interferometric Bidimensional Spectrometer (IBIS; Cavallini 2006), mounted at the Dunn Solar Telescope at the National Solar Observatory, NM, USA. High-order adaptive optics were applied throughout the observations (Rimmele 2004). IBIS acquired Na I D_1 spectral imaging with a spatial sampling of $0\farcs0976$ pixel^{-1}. The Na I D_1 line scan consists of 15 positions corresponding to a velocity range of -37 to $+34$ km s^{-1} (left panel of Figure 1). Speckle reconstruction was applied to the data (Wöger et al. 2008), utilizing $10 \rightarrow 1$ restorations. A full post-reconstruction IBIS scan through the Na I D_1 absorption profile had an acquisition time of 22.709 s, which is the effective cadence of the time series and includes a blueshift correction required due to the use of classical etalon mountings (Cauzzi et al. 2008). A movie of the observed flaring region at the line core (5895.89 Å), and in the blue wing (5895.76 Å) and red wing (5895.99 Å) is available online.

The flare was also observed by *RHESSI* (Lin et al. 2002). Hard X-ray (HXR) spectral analysis was performed using OSPEX (Schwartz et al. 2002) to estimate the power $P_{\rm nth}$ deposited in the chromosphere by the nonthermal electrons, assuming the thick-target model (Brown 1971).

3. ANALYSIS AND RESULTS

The two-ribbon M3.9 flare was observed in active region NOAA 12087 located at heliocentric coordinates $\sim(-755'', -297'')$. Figure 1 shows the flare images in the

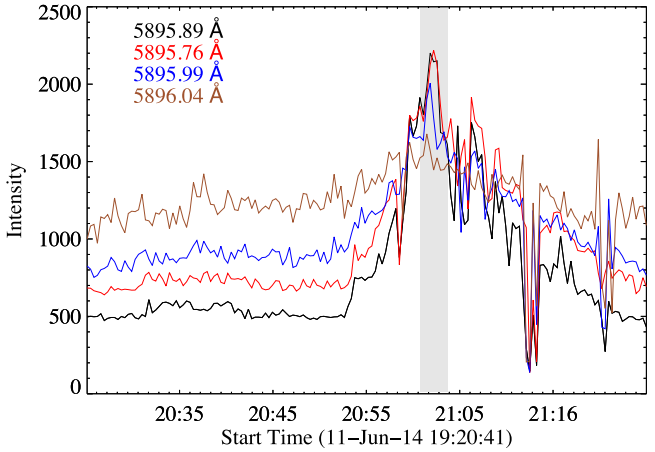

Figure 2. Light curves of the flaring region marked with the upper blue contour in Figure 1. The gray-shaded area indicates the time interval for which line profiles presented In Figures 3 and 4 are produced.

positions of the Na I D_1 line core and wings. Seeing was below average during the observations, but the flare-associated emission is clearly detected in the images. The temporal evolution of the flare at line core (5895.89 Å), blue wing (5895.76 Å), and red wing (5895.99 Å) is shown in the movie available online. Two bright ribbons are identified in the Na I D_1 images, highlighted with the blue contours in Figure 1. Light curves generated from the ribbon show the increase in the emission of the Na I D_1 core and wings, peaking at 21:04 UT (Figure 2).

In Figures 3 and 4 we show the Na I D_1 line profiles for the upper and lower ribbons respectively, averaged over the areas marked with the blue contour in Figure 1. The line profiles are produced during the flare peak, which is a vertical gray shade in Figure 2. Shortly after the flare onset, Na I D_1 rapidly appears in emission with a central reversal. Furthermore, the temporal evolution of the centrally reversed Na I D_1 profiles shows excess emission in the blue wing (blue asymmetry) with a nearly unshifted line center for most of the flaring profiles (Figures 3 and 4). After the flare maximum, from ~21:07 UT, the line profile gradually changes from the centrally reversed emission to the quiet pre-flare absorption.

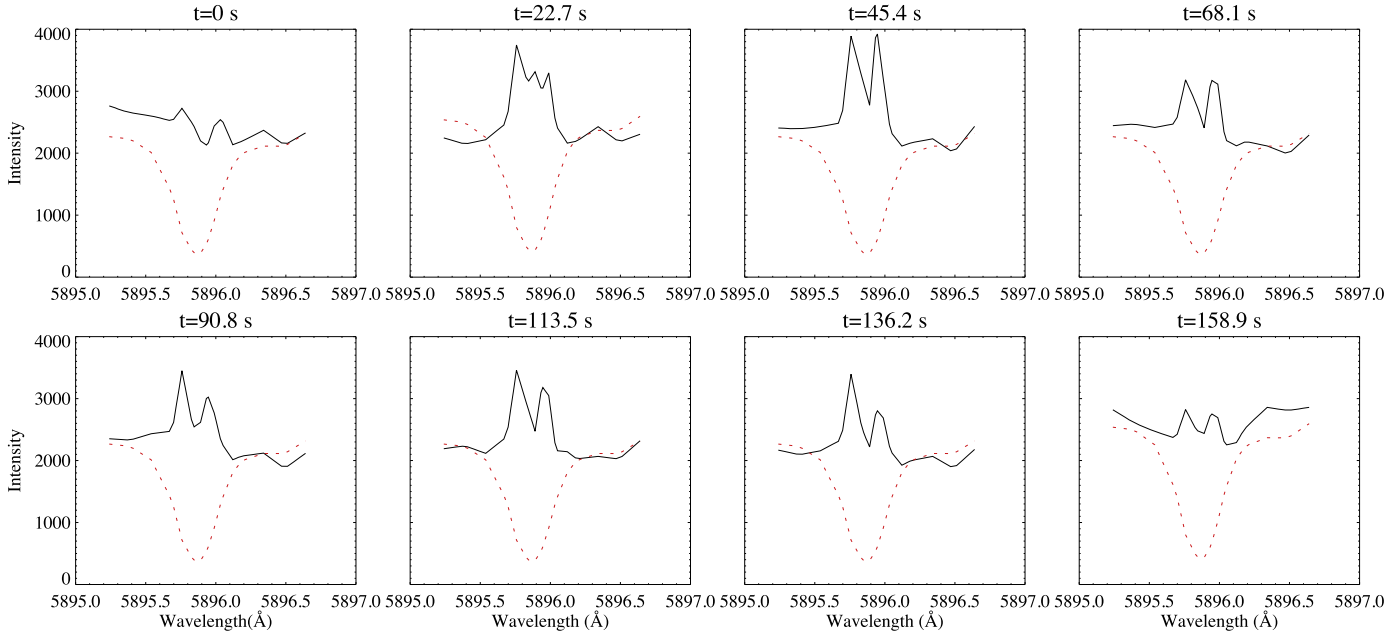

Figure 3. Temporal evolution of the Na I D_1 line profiles during flare maximum for the upper ribbon outlined with the blue contour in Figure 1. The profiles have been obtained from the temporal interval marked by the gray-shaded area in Figure 2. The red dashed lines show the mean spectrum averaged over the quiet Sun FOV for reference.

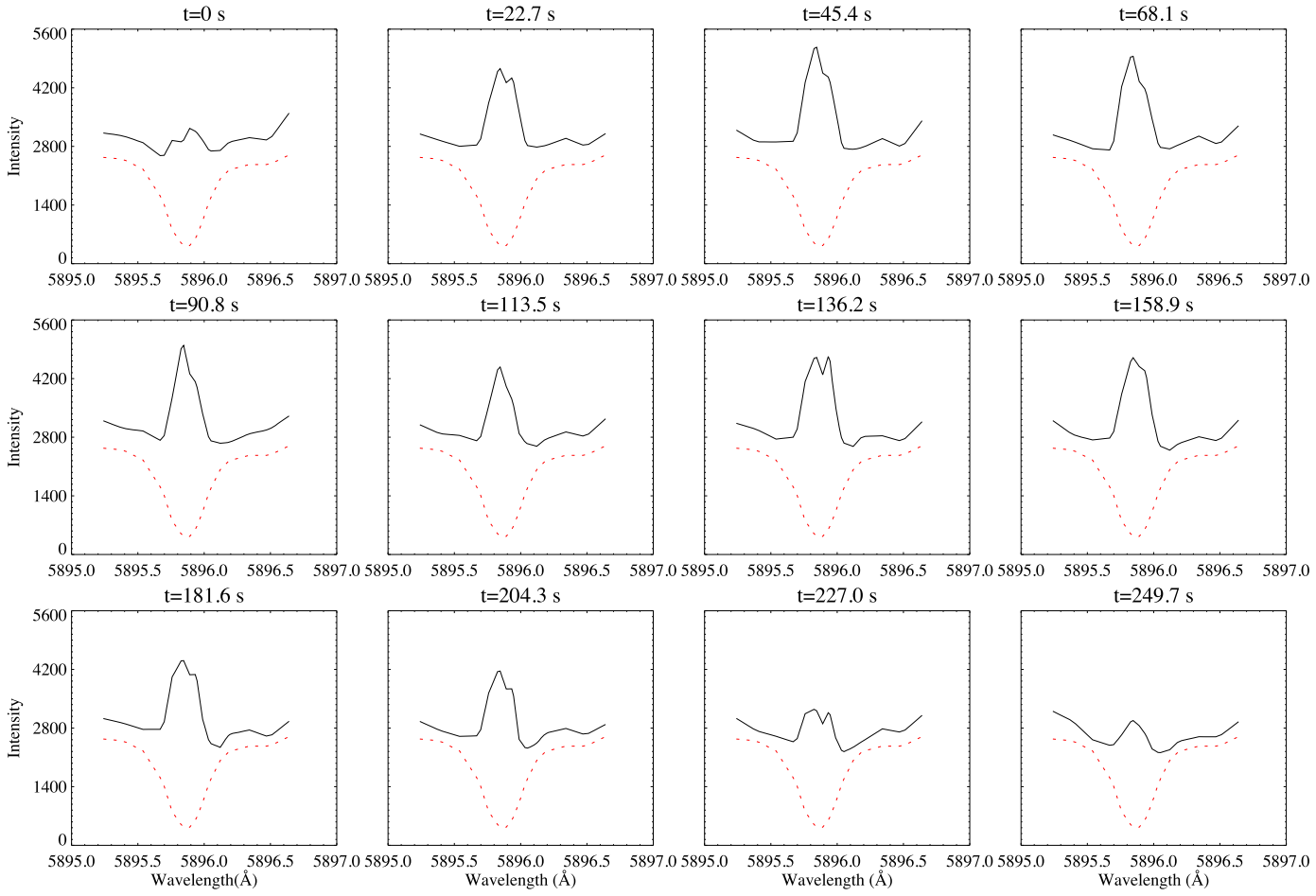

Figure 4. Same as Figure 3, except for the lower ribbon outlined with the blue contour in Figure 1.

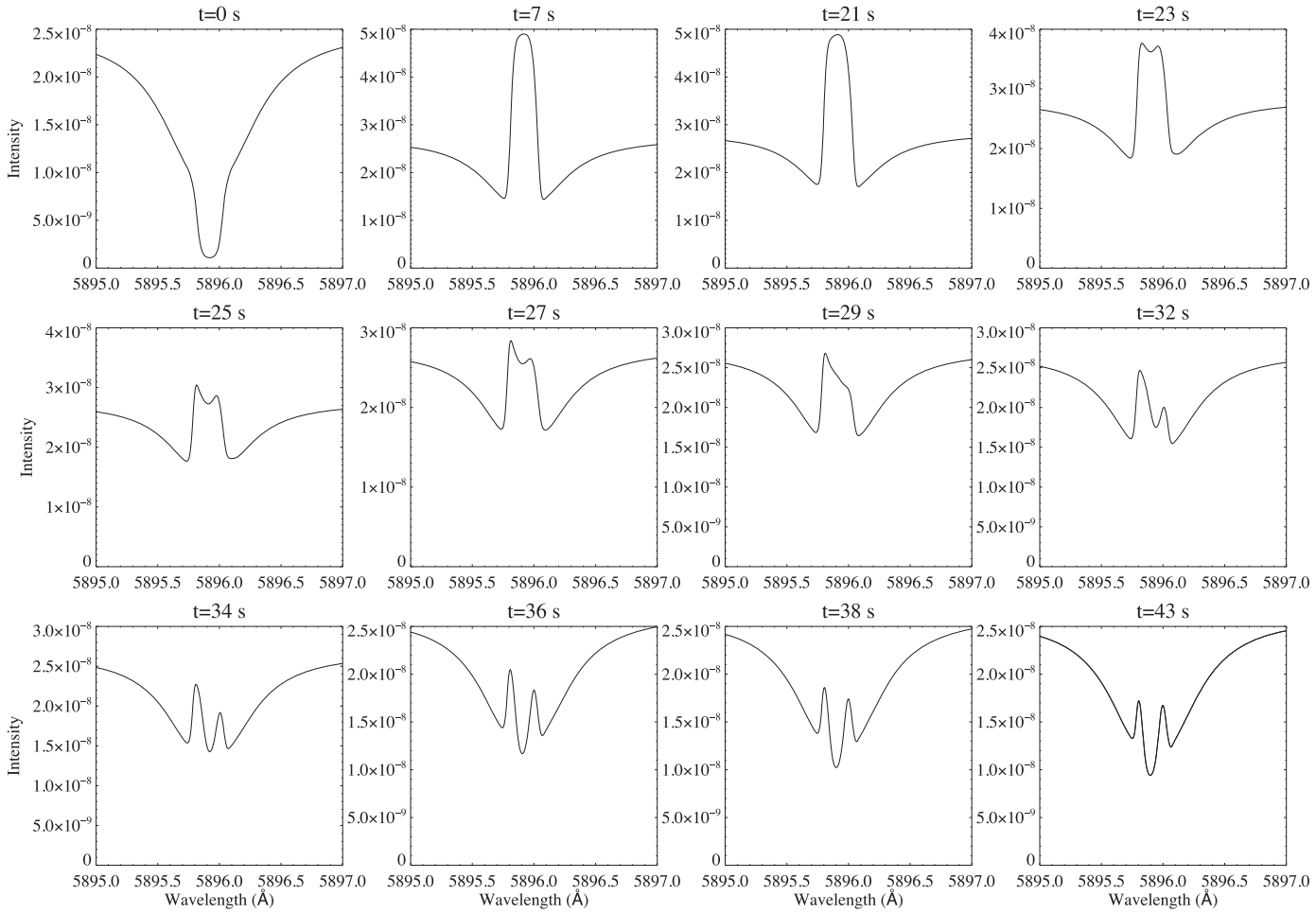

Figure 5. Temporal evolution of the synthesized Na I D_1 profile from the combined RADYN (F11) and RH simulations. A blue asymmetry is produced in the relaxation phase of flare simulation when the beam heating has ceased (after $t = 20$ s).

3.1. Hard X-Rays

The *RHESSI* data were fitted with an isothermal plus thick-target model, using the OSPEX function (`thick2_vnorm`), and they calculated $P_{\rm nth}$ throughout the impulsive phase, integrating the counts in bins of 12 s. *RHESSI* detectors 5 and 7 were employed because the results from the other detectors were too noisy to be used for a reliable fit. The spectral results give an estimate of the energy distribution $F(E)$ of the accelerated electrons during the flare, with total energy $P_{\rm th}$ derived by integrating the energy of the distribution of electrons $P_{\rm th} = \int EF(E)dE$. We found a maximum energy rate, $P_{\rm nth} \approx (3.6\text{–}5.5) \times 10^{28}$ erg s^{-1}, at the time of maximum of HXR emission. To obtain the energy flux (erg s^{-1} cm^{-2}) deposited into the chromospheric source, the power of the nonthermal electrons $P_{\rm nth}$ must be divided by the footpoint area. The reconstructed images for the HXR emission (using CLEAN, Hurford et al. 2002, detectors 3–8, beam width factor of 1.5) do not resolve the flare. However, the centroid of the HXR emission is well associated with the main locations of the Na I D_1 emission. Therefore, *RHESSI* images could not be used to estimate the size of the footpoints. The area of the ribbons was hence determined by contouring a region with intensity above 50% of the maximum of the image of the Na I D_1 5895.76 Å wing near the HXR peak, which gave a value of $\sim 10^{17}$ cm^2. Thus, at the time of the maximum HXR emission, the average energy flux delivered by the electrons into the chromosphere is around $(3.6\text{–}5.5) \times 10^{11}$ erg s^{-1} cm^{-2}.

3.2. Simulated Na I D_1 Line Profiles

To interpret the observational characteristics of Na I D_1 we generated synthetic line profiles with the radiative hydrodynamic code (RADYN; Carlsson & Stein 1997; Allred et al. 2005) and the radiative transfer code RH (Uitenbroek 2001). RADYN snapshots generated at different time steps can be used as an input atmosphere to RH to investigate the temporal evolution of the Na I D_1 line profile during the flare.

The RADYN simulation was performed for a strong beam with $F = 10^{11}$ erg cm^{-2} s^{-1} (also known as an F11 flare) and an isotropic pitch-angle distribution in the forward hemisphere with the Fokker–Planck solution to the nonthermal electron distribution (Allred et al. 2015). A constant heating flux was applied for 20 s, and the atmosphere was allowed to relax for an additional 40 s. We used a power-law index of $\delta = 4.2$ and a low-energy cutoff of $E_c = 25$ keV. Snapshots were produced and the Na I D_1 line profiles were synthesized for every single time step during the RADYN run of 60 s.

Figure 5 shows the temporal evolution of the synthesized Na I D_1 profiles from these combined simulations. Before the start of electron beam heating, at $t = 0$ s, the line is in absorption, but it changes rapidly into emission when the beam heating is initiated. The evolution of the temperature profile of

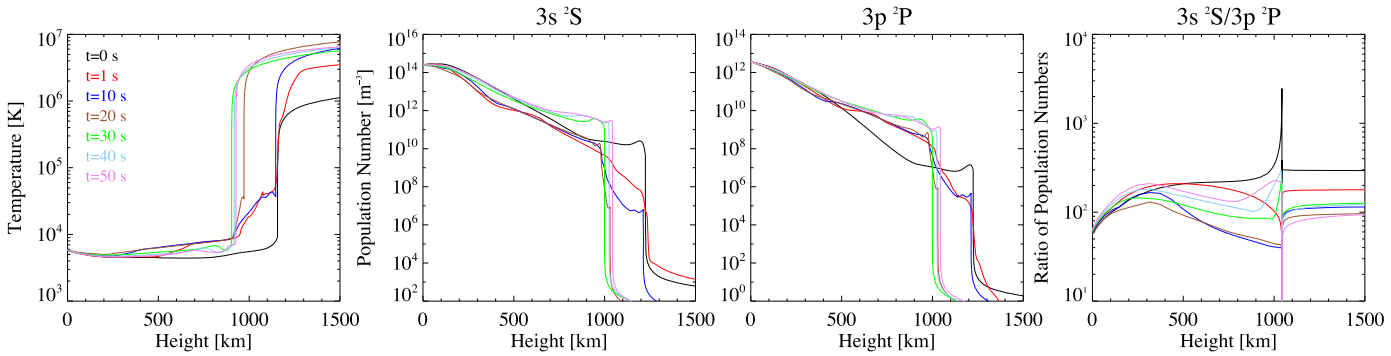

Figure 6. Temperature (left panel), the population density of the energy states 3s ^{2}S and 3p ^{2}P of the sodium atom (middle panels), and the ratio of the population densities of these two states (right panel) as a function of height at different stages of the simulation.

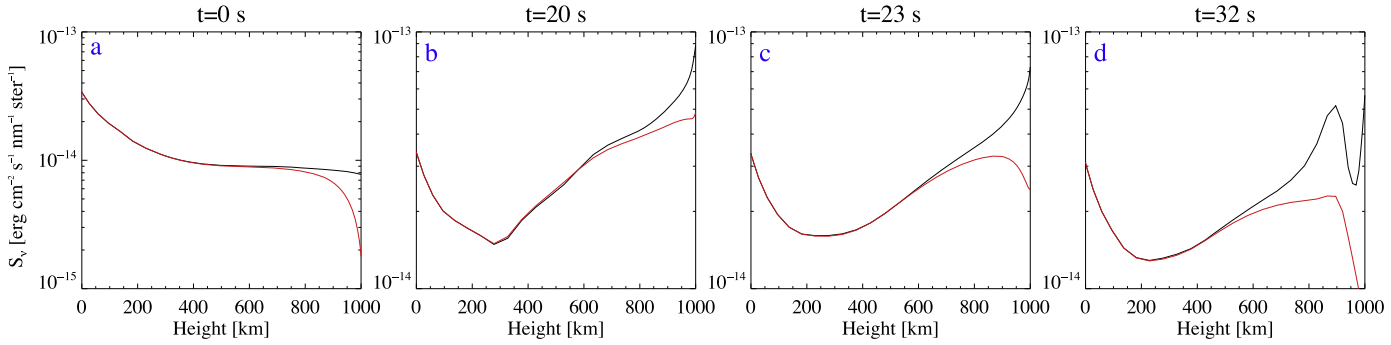

Figure 7. Temporal evolution of the source function (red lines) and Planck function (black lines) at Na I D_1 line center (5895.89 Å).

the flaring atmosphere shows that, following the beam heating ($t = 1$ s), the temperature increases from ~5000 K to ~7000–20,000 K at height ~500–1000 km (black and red lines of the left panel of Figure 6). The Na I D_1 and D_2 lines arise due to the 3s ^{2}S–3p $^2P_{1/2,3/2}$ transitions. The increased temperature leads to a rapid change in the population densities of these ^{2}S and ^{2}P states (middle and right panels of Figure 6). In particular, the population density of the Na I D_1 ground state (3s ^{2}S) is decreased at $t = 1$ s whereas the population of 3p ^{2}P is increased. The right panel of Figure 6 shows that the ratio of the population densities of the two states $^2S/^2P$ decreases by a factor of 10 during the first second of beam heating of the atmosphere at a height of around 500–1000 km. This beam heating increases the collisional rates and excites more electrons from the ground to the first excited state. In turn, this increases the probability that Na I D_1 photons, which previously would have been absorbed, escape freely and results in an increase in the line intensity.

We also investigate the line source function of the analyzed RH/RADYN run to study the temporal evolution of the radiation field of the Na I D_1 line. Figure 7 shows the source function at line center at different stages of the simulation. The Planck functions (black lines) are overplotted to show the height of non-LTE decoupling in the atmosphere. Before the start of electron beam heating, at $t = 0$ s, the source function decreases with increasing height and the resulting line profile is purely in absorption (panel (a) of Figure 7). However, during the beam heating at a height of ~300 km the source function, which in this region is strongly coupled to the Planck function, starts to increase the production of emission from the core formation region (panel (b) of Figure 7). The change in the source function, together with the change in the balance between the population densities of the energy states, switches the sodium line profile from absorption into emission. After 20 s, when beam heating was stopped, the temperature begins to decrease and the ratio of the population densities changes to the opposite direction (Figure 6). Furthermore, the line source function has developed a local maximum near the height of line core formation at around 900 km, where the source function is decoupled from the Planck function (panels (c) and (d) of Figure 7). As a result, Na I D_1 line profiles develop an absorption (central reversal) near the line core (Figure 5). Also, after the beam heating has ceased ($t = 20$ s), the centrally reversed Na I D_1 line profile shows excess emission in the blue wing (blue asymmetry) with nearly unshifted line center (see panels (d)–(h) of Figure 8). This is similar to the observed line profiles.

To understand the formation of the asymmetric line profiles, we need to examine the line contribution functions (Carlsson & Stein 1997). These are the intensities emitted at specific wavelengths from specific heights, introduced as a formal solution of the radiative transfer equation for the emergent intensity. Carlsson & Stein (1997) investigated the formation of optically thick spectral line asymmetries using RADYN simulations. They showed that these asymmetries are produced by the velocity gradients near the formation height of the spectral line profile. In particular, if the velocity decreases outward (negative velocity gradient), then higher-lying atoms absorb at longer wavelengths (red photons), so the opacity at greater heights is smaller on the blue side of the line profile and a blue asymmetry is formed. Whereas, if the velocity increases outward (positive velocity gradient), higher-lying atoms absorb at shorter wavelengths (blue photons) and the opacity is smaller on the red side of the line.

In Figure 8 we present the temporal evolution of the contribution functions for the Na I D_1 line. The diagrams are

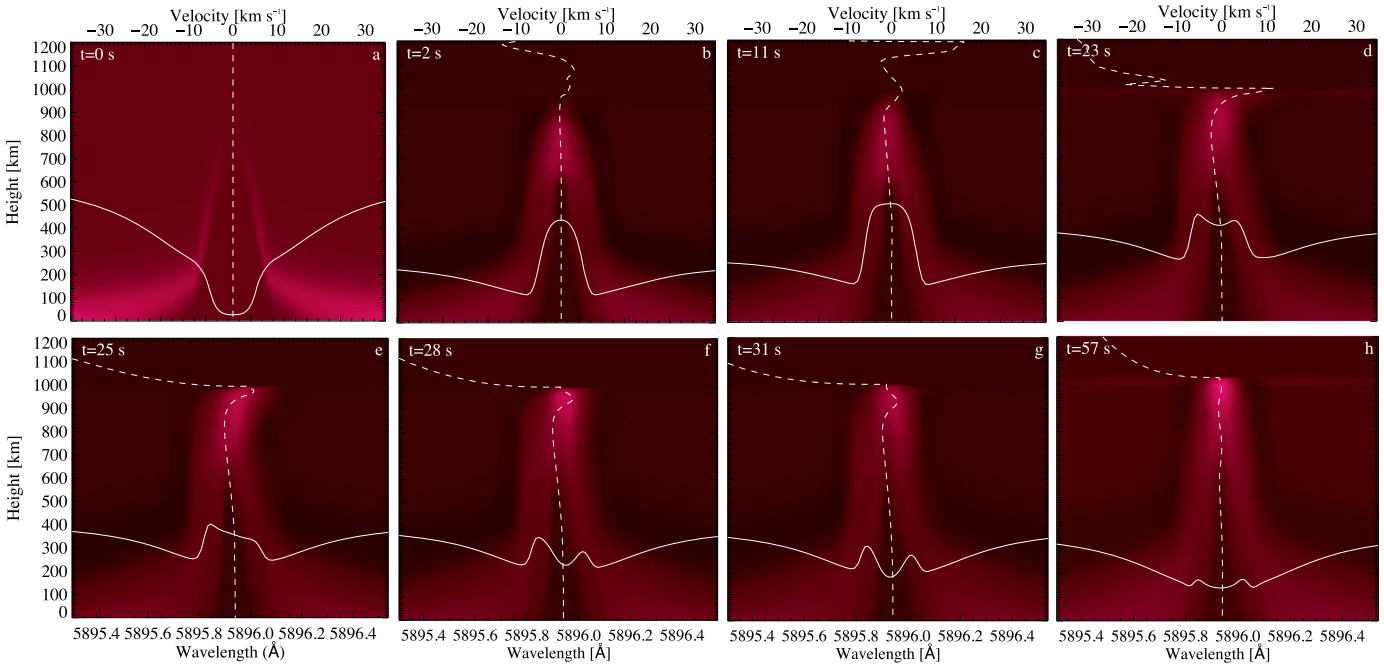

Figure 8. Intensity contribution function for the Na I D_1 line at different stages of the simulation. The diagrams are plotted on a red scale so that brighter shades indicate higher intensities. The line profile is overplotted as a full white line. The vertical velocity structure of the plasma is overplotted as a white dashed line (negative velocity corresponds to plasma upflows).

plotted on a red color scale, with brighter shades showing higher intensities. Line profiles are shown as white solid lines, while the vertical velocity structure is plotted as a red dashed line. We note that positive values for velocities correspond to plasma downflows.

The contribution function diagram at $t = 0$ shows that the Na I D_1 line core is formed at a height of ∼400–900 km in the non-flaring, static atmosphere (panel (a) of Figure 8). Although the electron beam disturbs the velocity field due to the nonthermal heating, during the first few seconds the field at the Na I D_1 formation height is still undisturbed. This is because the primary site of energy release, where strong upflows (evaporations) and downflows (condensations) are generated, is located above the formation layer for the Na I D_1 line (Figure 8). Therefore, the Na I D_1 line profile is still symmetric with respect to the line core. However, from $t = 20$ s the lower atmosphere also has developed a weak upflow of about 2–3 km s^{-1} (panel (d) of Figure 8). At ∼400–800 km, where most of the line emission core is formed, the velocity gradient with respect to the height outward is negative (i.e., velocity decreases outward). As mentioned earlier, the negative velocity gradient shifts the wavelength of maximum opacity to the red. The higher-lying plasma of the line core absorbs red photons, increasing opacity in the red wing. This makes the height range over which the contribution function is high greater in the blue wing of the profile, and the blue asymmetry is established (panel (d) of Figure 8). The cores of the simulated Na I D_1 profiles remain unshifted when the blue asymmetry is detected (panels (d), (e), (f) of Figure 8). This may be due to the presence of different velocity fields with positive gradients between ∼850–950 km, which produce an effectively unshifted line core. The structure of the velocity field does not change during the next ∼20 s, and hence the blue asymmetry is maintained (panels (e), (f), (g) of Figure 8). After around 50 s, the velocity field becomes very weak and the line profile establishes a symmetric shape again (panel (h) of Figure 8).

3.3. Hα *versus* Na I D_1 *line*

The RADYN simulations used to synthesize the Na I D_1 line were also employed by Kuridze et al. (2015) to study the evolution of the Hα line profile of the flaring atmosphere. In the F11 RADYN model, the Hα line is formed at a height of ∼900–1200 km and hence could be used as a diagnostic of the chromosphere at heights above that of Na I D_1 formation (∼400–900 km; Section 3.2). Our analysis revealed that approximately 7–8 s after the beam heating has started, Hα shows excess emission in the blue wing (blue asymmetry) with a redshifted line core. At 20 s, the beam heating maintains a temperature of ∼10,000–35,000 K (Figure 8). This region shows a downflow velocity of ∼10–15 km s^{-1}, with the downflow formed at $t = 6$–7 s). When the beam switches off (at 20.01 s), the temperature in the region drops to $T \sim 11{,}000$ K from $T \sim 35{,}000$ K in 0.1 s. The pressure ratio between the material that suddenly cooled ($P_{\rm below\ TR}$) and the maximum pressure in the flare transition region ($P_{\rm TR}$) changes rapidly: $P_{\rm TR}/P_{\rm below\ TR}$ increases. This drives another downflow at a higher velocity of $v \sim 20$–25 km s^{-1}. The two downflows are cooling rapidly as this material increases in density, while the beam heating is no longer present to slow the cooling. Material just below the flare transition region decreases in velocity, while the temperature decreases to 6500–7000 K at $t = 27$ s. Thus, the downflowing material is sufficiently hot to excite the $n = 2$ level of hydrogen when the beam heating is on ($t < 20$ s).

On the other hand, for $t < 20$ s the temperature of the material at lower heights (∼400–850 km), which does not have appreciable velocity (small upflows), is ∼7000–7700 K and it emits in Na I D_1 (Figure 8). However, when the beam heating turns off, the temperature in this region drops, with the value of

the drop increasing with height in this range. Therefore the pressure ratio between the material in the upper and lower areas in the ~400–850 km region decreases. This drives the upflow with a velocity of $v \sim 2$–$3\ \mathrm{km\ s^{-1}}$, which in turn produces the blue asymmetry in the Na I D_1 line profie.

4. DISCUSSION AND CONCLUSION

We have presented spectroscopic observations of the Na I D_1 line in an M3.9 flare and compared our findings with radiative hydrodynamic simulations. Our observations at high spectral resolution show that during the flare the Na I D_1 line goes into emission and a central reversal is formed (Figures 3 and 4). The analysis of synthetic line profiles indicates that the change from absorption to emission is a result of the heating of the lower solar atmosphere by the nonthermal electron beam. Although the formation of the line occurs deep below the primary site of nonthermal energy dissipation, it is still strongly affected by the heating because the temperature of the region responds immediately to the electron beam (left panel of Figure 6). The heating rapidly changes the balance between the population densities of the energy states in the sodium atom (Figure 6), with increased collision rates exciting electrons from the ground ^{2}S to the first excited state ^{2}P, which allows Na I D_1 photons to escape freely and results in an increase in the line intensity. Furthermore, the line source function shows a local minimum near 300 km and increases toward the core formation height (Figure 7). As a result, during the heating phase the line profile developes fully into emission. However, when the beam heating is stopped the temperature starts to drop and the ratio of the population densities changes back again (Figure 6). The line source function has developed a local maximum near 900 km, in the region where the source function is already decoupled from the Planck function. As a result, the line profiles develop a small absorption near the line core (central reversal), as shown in Figure 5. The observed line profiles have similar centrally reversed shapes during the flare (Figures 3 and 4), with the absorption dip smaller for the lower ribbon profiles, indicating that the heating was more intense in the lower ribbon (Figures 3 and 4). Indeed, RH simulation confirms that in the flaring atmosphere produced with the lower electron flux (e.g., F9 model), the Na I D_1 profile has a deeper absorption dip in the relaxation phase.

It must be noted that the central reversal in the synthetic Na I D_1 line profile appears only after heating ends, i.e., in the relaxation phase of the flare simulation. During the beam heating the line profile develops fully into emission without reversal. Recent ground-based observations of solar flares at high spatial resolution in the Hα and He I 10830 Å lines indicate that the ribbon kernels of M-class solar flares could have very narrow widths, <500 km (Sharykin & Kosovichev 2014; Jing et al. 2016; Xu et al. 2016). This suggests that the actual footpoint size of the flaring loops could be smaller, and hence the energy flux could be higher than the estimated $10^{11}\ \mathrm{erg\ s^{-1}\ cm^{-2}}$. To assess the effects of a higher energy input on the synthesized Na I D_1 line profile we performed RADYN simulations for a stronger ($5 \times$ F11) energy flux (Kowalski et al. 2016) and used the resulting atmospheric snapshots in RH for synthesizing Na I D_1 line profiles. The resulting line profiles show a similar evolution pattern. When beam heating is turned on the Na I D_1 line is in total emission (without a central reversal). When the beam heating is turned off the line profiles become centrally reversed with asymmetric wing emission, which depends on the velocity field. Similar behavior has been shown by the synthesized Na I D_1 spectra simulated with RH for a weaker (F9) RADYN atmosphere. Therefore, the response of the atmosphere at the Na I D_1 formation height to the different energy beam heatings is qualitatively similar. This shows that the formation of the central reversal in the spectra could be used as a diagnostic of the nonthermal heating processes in solar flares.

The temporal evolution of the line profile shows excess emission in the blue wing with an almost unshifted line core (Figures 3 and 4). In an atmosphere without velocity fields, the centrally reversed chromospheric line profiles are symmetric with respect to the line core (Fang et al. 1993; Cheng et al. 2006). However, dynamic models account for the mass motions of the flaring material and reproduce the asymmetric signatures seen in the observations. Our Figure 8 shows that in a zero velocity field the line profile is indeed symmetric. The velocity field in the lower solar atmosphere is not disturbed during the first 10 s of the active beam heating that produces the explosive evaporation above 1000 km, which is higher than the line formation height. However, after 20 s the lower atmosphere has developed upflows of around 2–$3\ \mathrm{km\ s^{-1}}$, which are generally attributed to gentle evaporation. As a result, the symmetry in the line profiles is now broken. The negative velocity gradient at around 400–800 km modifies the optical depth of the atmosphere in such a way that higher-lying (core) atoms absorb photons with longer wavelengths (red wing photons) and the blue asymmetry is formed (Figure 8).

The line cores of the observed and simulated Na I D_1 asymmetric line profiles remain unshifted (panels (d), (e), (f) of Figure 8), in contrast to the centrally reversed Hα line profiles, which show a redshifted line core during the blue asymmetry (Kuridze et al. 2015). This may be due to more complex velocity fields with different condensation/evaporation patterns. Indeed, Figure 8 shows that the velocity gradient changes sign above 800 km, which covers the upper, narrow layer of core formation. This can produce an effectively unshifted line core.

To our knowledge, we have presented the first imaging spectroscopy at high spectral resolution of a solar flare in the Na I D_1 line. The simulated line profiles show good agreement with observations, indicating that they can be a very important diagnostic of the properties and dynamics of the lower flaring atmosphere located below the formation height of the Hα and Ca II line cores. We have shown that, as in Hα, the asymmetries in centrally reversed Na I D_1 spectral profiles could be an effective tracer of the velocity field in the flaring atmosphere.

The Dunn Solar Telescope at Sacramento Peak/NM is operated by the National Solar Observatory (NSO). NSO is operated by the Association of Universities for Research in Astronomy (AURA), Inc. under cooperative agreement with the National Science Foundation (NSF). The research leading to these results has received funding from the European Community's Seventh Framework Programme (FP7/2007-2013) under grant agreement No. 606862 (F-CHROMA).

REFERENCES

Abbett, W. P., & Hawley, S. L. 1999, ApJ, 521, 906
Allred, J. C., Hawley, S. L., Abbett, W. P., & Carlsson, M. 2005, ApJ, 630, 573
Allred, J. C., Kowalski, A. F., & Carlsson, M. 2015, ApJ, 809, 104
Brown, J. C. 1971, SoPh, 18, 489
Carlsson, M., & Stein, R. F. 1997, ApJ, 481, 500

Cauzzi, G., Reardon, K. P., Uitenbroek, H., et al. 2008, A&A, 480, 515
Cavallini, F. 2006, SoPh, 236, 415
Cessateur, G., Kretzschmar, M., Dudok de Wit, T., & Boumier, P. 2010, SoPh, 263, 153
Cheng, J. X., Ding, M. D., & Li, J. P. 2006, ApJ, 653, 733
de la Beaujardière, J.-F., Kiplinger, A. L., & Canfield, R. C. 1992, ApJ, 401, 761
Falchi, A., Falciani, R., & Smaldone, L. A. 1990, A&AS, 84, 601
Fang, C., Henoux, J. C., & Gan, W. Q. 1993, A&A, 274, 917
Finsterle, W., Jefferies, S. M., Cacciani, A., Rapex, P., & McIntosh, S. W. 2004, ApJL, 613, L185
Gurtovenko, E. A. 1967, SoPh, 1, 389
Hurford, G. J., Schmahl, E. J., Schwartz, R. A., et al. 2002, SoPh, 210, 61
Ichimoto, K., & Kurokawa, H. 1984, SoPh, 93, 105
Jess, D. B., Mathioudakis, M., Christian, D. J., Crockett, P. J., & Keenan, F. P. 2010, ApJL, 719, L134
Jing, J., Xu, Y., Cao, W., et al. 2016, NatSR, 6, 24319
Kowalski, A. F., Daw, J. C., Cauzzi, G., & Carlsson, M. 2016, ApJ, submitted (arXiv:1609.07390)
Kuridze, D., Mathioudakis, M., Simões, P. J. A., et al. 2015, ApJ, 813, 125
Leenaarts, J., Rutten, R. J., Reardon, K., Carlsson, M., & Hansteen, V. 2010, ApJ, 709, 1362
Lin, R. P., Dennis, B. R., Hurford, G. J., et al. 2002, SoPh, 210, 3
Montes, D., Sanz-Forcada, J., Fernandez-Figueroa, M. J., & Lorente, R. 1996, A&A, 310, L29
Moretti, P. F., Andretta, V., Cacciani, A., et al. 2002, in Proc. ESA Special Publication 477, Second Solar Cycle and Space Weather Euroconference, ed. H. Sawaya-Lacoste (Noordwijk: ESA), 147
Rimmele, T. R. 2004, Proc. SPIE, 5490, 34
Schwartz, R. A., Csillaghy, A., Tolbert, A. K., et al. 2002, SoPh, 210, 165
Sharykin, I. N., & Kosovichev, A. G. 2014, ApJL, 788, L18
Simoniello, R., Jiménez-Reyes, S. J., García, R. A., & Pallé, P. L. 2008, AN, 329, 494
Uitenbroek, H. 2001, ApJ, 557, 389
Wöger, F., von der Lühe, O., & Reardon, K. 2008, A&A, 488, 375
Wuelser, J.-P., & Marti, H. 1989, ApJ, 341, 1088
Xu, Y., Cao, W., Ding, M., et al. 2016, ApJ, 819, 89